Research paper

New radio-seismic indicator for ELF seismic precursors detectability

Andrea Mariscotti [a,*], Renato Romero [b]

[a] *University of Genoa, Via Opera Pia 11A, 16145 Genova, Italy*
[b] *Independent researcher, Str. Luisetti 12, 10040 Cumiana (TO), Italy*

ARTICLE INFO

ABSTRACT

This work considers the effectiveness of earthquakes (EQs) radio precursors mainly in the Extremely Low Frequency (ELF) range and below, and carries out an analysis based on a comprehensive set of EQ events documented in past publications and provided by the Opera 2015 project (six stations located in Italy). A new Radio-Seismic Indicator (RSI) is proposed, with the magnitude-distance relationship physically justified by path-loss expressions of the transverse magnetic mode. Classification performances of past and proposed RSIs are assessed calculating confusion matrices and on those the balanced accuracy and Matthews' coefficient: the RSI performs significantly better reducing fall-outs and increasing precision for both classes, positive and negative precursors. Performance improvement is inherently limited by the overlap of the classes.

1. Introduction

During an earthquake (EQ) event, and also before it, low-frequency (LF) electromagnetic (e.m.) emissions would be generated that are detectable by stations on the Earth's surface. These e.m. waves of seismomagnetic (dependency of the electromagnetic properties of rocks on stress) or electrokinetic (various effects caused by movement and flows due to pressure changes) origin Johnston et al. (1981) may be exploited as precursors (named often "radio precursors") to predict EQ events. There are different opinions on detectability of such precursors, ranging from a skeptical standpoint to a full endorsement of a world-wide detectability, at least for the most intense EQs, in the order of Richter magnitude $M = 6$ or above (Fraser-Smith and Bannister, 1998; Bannister, 1984; Shrivastava, 2014; Akinaga et al., 2000; Schekotov et al., 2013; Hattori, 2004a; Chauhan et al., 2012; Straser, 2012; Straser and Cataldi, 2014; Straser, 2011; Contoyiannis et al., 2016; Heavlin et al., 2022).

Works on precursors of e.m. nature are many, focusing in the last ten-twenty years on various signal processing and statistical techniques (Febriani et al., 2014; Hattori et al., 2006), exploring in particular the ELF range (ITU-T Std. B.15, 1996), expected to better characterize natural phenomena of this kind and to propagate at longer distances. The received intensity is very low and many noise sources may affect magnetic and electric field measurements: external fields of human origin; thermal noise and thermocouple effect at connectors, cables and in general circuit junctions; atmospheric events and in particular thunderstorms; movement of magnetic coils in the static Earth's field caused by vibrations.

A common starting point for the interpretation of received signals and identification of precursors is ensuring a minimum signal-to-noise ratio at receiving instruments, whatever the post-processing technique. Noise should include natural sources and man-made noise. The consequence is that two factors can be identified as favoring detectability of precursor components in the received signals: the intensity of the earthquake (EQ) and the relative distance R from the measuring station. If we attribute to a given magnitude an arbitrary amount of e.m. energy, a path loss estimate (having defined a model for the attenuation versus distance of the e.m. waves) indicates the expected EQ signal power and the possibility of receiving a precursor signal.

The objectives of this work are: (i) Deriving a RSI expression from the equations of the e.m. field propagation in the frequency range of interest. (ii) Making available a comprehensive dataset of observations, mostly of the last 20 years, that report positive or negative detection of EQ events with quantitative information on intensity, location and analyzed frequency range; the events recorded during the Opera 2015 Project (Romero et al., 2023) are included. (iii) Verification of the proposed RSI and other similar indicators against the EQ dataset using visual and statistical techniques to measure the ability to classify the observations.

The paper is thus structured introducing the propagation at ELF in Section 2: the RSI equation is derived and compared to other published indicators. The review of the reported seismic events appears in Section 3, where the details are given of those accompanied by information on the observed precursors in terms of frequency band and intensity. Section 3 shows also the results obtained with the Opera 2015

---

* Corresponding author.
E-mail address: andrea.mariscotti@unige.it (A. Mariscotti).

Table 1
Original H_ϕ calculation parameters (Li and Pan, 2014).

Parameter	Value
Earth's radius	6370 km
Current moment of the dipole	1 Am
Ground conductivity	10^{-4} S/m
Ionosphere conductivity	10^{-5} S/m
Ionosphere equivalent reflection height	70 km

project for six radio-seismic measuring stations spread all over Italy. The collected events are then classified in Section 4, using the examined indicators and reporting considerations on detectability, as well as the consistency of collected data. Section 5 is the conclusion of this paper.

2. Materials and methods

2.1. Radio waves sources and propagation

Propagation of e.m. waves through the ground is favored by its wavelength: if precursor waves are generated at depth, then components at sufficiently low frequency will be able to emerge at the surface. In most cases the measuring station will be located in the reactive field region. For both electric and magnetic field components attenuation with distance R can be separated as: isotropic e.m. attenuation as in free space (as $1/R$), and magnetic/electric field attenuation in the reactive region (as $1/R^3$ and $1/R^2$) (Watt, 1967; Bannister et al., 1973).

The crust and Earth's surface are part of a spherical shell that is top bounded by the lower part of the ionosphere forming a sort of waveguide, known as Earth-ionosphere Waveguide (EIWG). Various models have been developed for the propagation of e.m. waves along it, in particular for Very Low Frequency (3 kHz to 30 kHz) long-distance radio transmission (Bahar and Wait, 1965). At a first approximation the reflection coefficients at both the Earth's surface and first ionosphere level may be assumed unitary. To excite propagation in the waveguide various sources may be modeled as vertical electric dipole (VED) and horizontal electric dipole, as discussed in Wait (1960), Peng et al. (2012), Li and Pan (2014).

A VED source is usually considered (Wait, 1960; Hattori et al., 2006), that in spherical coordinates has electric field in the radial r direction (vertical to Earth's surface) and electric and magnetic field in the angular direction θ and ϕ, respectively, formulated in Wait (1960) for the VLF range, and refined by Li and Pan (2014) for the SLF/ELF range. With a wavelength longer or comparable to the Earth's circumference, the TM mode eigenvalue is never much greater than one for frequencies below about 50 Hz, condition that covers the vast majority of the observed precursors (see Section 3).

The expressions of H_ϕ derived in Li and Pan (2014), sec. 2.2.4, between 1 Hz and 20 Hz are plotted in Fig. 1 and will be used in Section 2.4.1 to derive an approximate law of propagation. The parameters taken from Li and Pan (2014) for the calculation of H_ϕ are listed in Table 1.

H_ϕ path loss curves are shown in Fig. 1 as separate curves (c_1, c_2, c_3, c_4) at each of the four listed frequencies (1, 5, 10 and 20 Hz) and as average of some curves (c_{123}, c_{23} and c_{234}) with obvious meaning of notation. These average curves aim at bracketing the most relevant intervals and discard selectively the first and the last that have quite opposite behavior. The 5–10 Hz interval (c_{23}) is included to selectively capture Schumann's resonance. The intention in Section 2.4.1 is to apply curve fitting to selected frequencies and on these verify predictive capability for events measured at the same or similar frequency intervals.
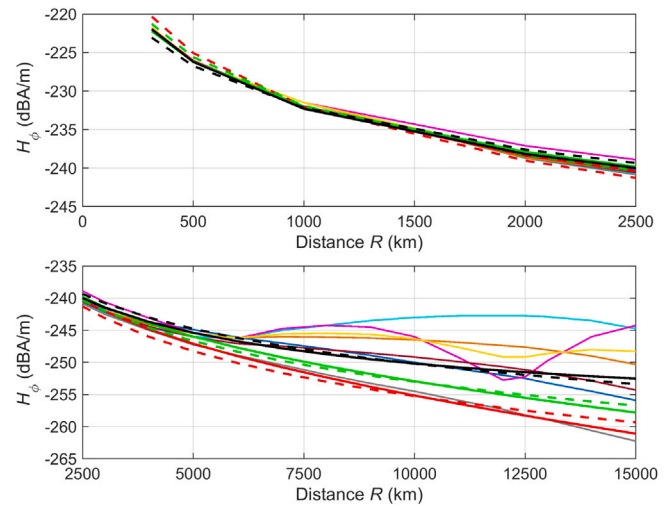

Fig. 1. Path loss curves vs. distance for H_ϕ at frequency values characteristics of ELF range. Cold colors for original H_ϕ values (Li and Pan, 2014): 1 Hz (grey), 5 Hz (light blue), 10 Hz (cyan) and 20 Hz (purple); hot colors for combined average curves covering 1 Hz to 10 Hz (brown), 5 Hz to 10 Hz (light brown) and 5 Hz to 20 Hz (orange). Red, green and black dashed and solid curves represent interpolation of first- and second-order path-loss models, as in Section 2.4: c_1 (1 Hz) red, c_{12} (1 Hz to 5 Hz) green, c_{123} (1 Hz to 10 Hz) black.

Table 2
EQ energy-magnitude semi-empirical formulas.

Expression	Source
$\log_{10} E = 5.24 + 1.44M$	Bath (1966)
$\log_{10} E = 4.8 + 1.5M$	Bormann and Giacomo (2010)[a]
$KKI = 10^{1.5M-K}$ [b]	University of California, Los Angeles (2017)

[a] Referred to as "Gutenberg–Richter-Kanamori".
[b] The energy may be expressed in kton of TNT (with the so called Kelly Kiloton Index, KKI), giving rise to an equivalence between earthquakes and other events with large energy release; $K = 3, 6, 9$ for unit of measure of KKI in ton, kton and Mton, respectively.

2.2. Earthquake energy as source intensity

The RSI quantity is derived using an estimate of the earthquake (EQ) power, suitable to identify the conditions for the detectability of precursors. The EQ energy E can be derived from the magnitude M by using semi-empirical formulas, summarized in Table 2.

The EQ energy is delivered during the evolution of the seismic event. It is assumed that an average power can be used and it is representative of it, as related to the duration of the e.m. waves, recorded usually for some seconds. The intensity of the source to feed into the wave propagation equations can thus be trimmed to the square root of this average power.

2.3. Overview of published indicators

The hypothesis that a stronger EQ will be preceded by stronger precursors, and that being close to the epicenter offers better opportunities to detect the precursors, is quite logical and already commented by Hattori (2004a). He showed in his conclusions that the detectable distance R_{det} (in km) should satisfy the inequality

$$R_{det} < 40(M - 4.5) \tag{1}$$

Molchanov et al. (2005) proposed the KS index, that is reported in a variety of forms, with and without a "+100" and with and without a 10× factor at the denominator:

$$K_{S1} = \frac{10^{0.75M}}{10R} \quad K_{S2} = \frac{10^{0.75M}}{R + 100} \quad K_{S3} = \frac{10^{0.75M}}{10(R + 100)} \tag{2}$$

where M is the magnitude of the EQ and R is the distance from the epicenter in km. K_{S1} is reported by Hayakawa et al. (2012), where the criterion of $K_{S1} > 1$ is clearly stated, for the possibility of detecting seismic precursors. K_{S2} is shown in Ohta et al. (2013) and it is understood that it is an adjustment for short distances, to take into account the hypocenter position with respect to the epicenter at the surface and the increased distance. Fig. 2 in Ohta et al. (2013) also implicitly indicates a $K_{S2} > 1$ criterion, as a horizontal line at 1 is drawn with the relevant events positioned slightly above it. K_{S3} is reported in Schekotov et al. (2020) without other details.

Hattori et al. (2006) and Han et al. (2017) consider the daily sum E_s of the local earthquake energy E'_s (indicating with R the distance from the epicenter):

$$E_s = \sum_{1\ \text{day}} E'_s \qquad E'_s = \frac{10^{4.8+1.5M}}{R^2} \tag{3}$$

A threshold of 10^8 for E_s is set for detectability of ULF magnetic anomalies. As pointed out in Han et al. (2017), for a magnitude $M = 4$, the hypocenter should be closer than $25\,\text{km}$, of course considering one event only in the whole day. In general, one event is prevailing on the others of the same day and also considering evaluations over time intervals shorter than one day, the criterion may be applied directly to E'_s.

Fraser-Smith et al. (1990) indicate an empirical threshold that is linear in the magnitude M and distance R, but is just a rewriting of the previous Hattori's R_{det} in (1):

$$0.025R = M - 4.5 \tag{4}$$

Han et al. (2017, Sec. 5.3) gives another criterion for detectability, calculating the probability of detection as a function of distance, using Molchan's error diagrams and focusing on distances of $100\,\text{km}$ to $200\,\text{km}$. The authors justify a lower probability for longer distance observing that a larger radius around the monitoring station "may bring in irrelevant events that do not produce detectable magnetic anomalies, thereby increasing the missing rate" A clear threshold is not given, but $100\,\text{km}$ is identified as an ideal reference distance for good detectability.

A preliminary RSI abbreviated with the notation "RI" was proposed in Romero et al. (2023) using the terms $10^{1.5M}$ for the energy and $R^{1.5}$ as attenuation law with distance (intermediate between the first and second order terms discussed below). Using a different scaling, the thresholds for detectability were located at $10\,\text{dBe}$ and $30\,\text{dBe}$ for negative and positive precursors, with an "gray" area with some mixed negative and positive events.

2.4. Fitted path loss relating H_ϕ with distance R

As preliminarily observed for the H_ϕ curves of Fig. 1, the resulting best fit is a trade-off between quite different curves: there are thus slightly different RSI curves for different frequency intervals, with preference for interval c_1. Fitting is based on minimization of the mean square error (MSE) considering both first-order and second-order path-loss models; the reason is the evident change of concavity of the original curves shown in Fig. 1. A two-term path-loss is able to follow the change of slope for the quite extended distance range. Fitting curves are shown splitting the interval into distances up to $2500\,\text{km}$ and above it (it is remarked that for long distances the identified events are few).

$$\begin{aligned} PL_1 &= -20\log_{10}(R^{p_1}) - q \\ PL_2 &= -20\log_{10}(a_1 R^{p_1} + R^{p_2}) - q \end{aligned} \tag{5}$$

where R is the distance (in km) between the event and the observer; p_1 and p_2 are the path-loss exponents, q is the intercept (providing vertical adjustment with respect to H_ϕ values) and a_1 ensures continuity between the two power terms.

The overall behavior is summarized quantitatively in Table 3 and graphically represented earlier in Fig. 1, by giving the fitting performance for various portions of the ELF frequency interval: c_1 (1 Hz),

Table 3
Results of path-loss curve fitting.

Ref. curve 1	q	p_1	a_1	p_2	MSE (dB)
c_1 (1 Hz)	162.428	1.160	—	—	25.99
c_{12} (1–5 Hz)	168.676	1.054	—	—	14.21
c_{123} (1–10 Hz)	178.070	0.902	—	—	17.19
c_1 (1 Hz)	171.700	2.853	1.633E−08	1.007	4.29
c_{12} (1–5 Hz)	173.968	2.773	1.214E−08	0.967	6.39
c_{123} (1–10 Hz)	182.282	1.237	−0.829	1.220	10.38

c_{12} (1–5 Hz) and c_{123} (1–10 Hz). To obtain per-event MSE values, those reported in Table 3 must be divided by the total number of positive and negative events, namely 126. As graphically demonstrated in Fig. 1, fitting is quite good, especially for the second-order model.

Higher frequencies than in this study are considered in Fraser-Smith and Bannister (1998) and results there confirm that the model of propagation obtained by the solution of field equations is quite accurate and matches experimental data of several months of year 1990 at $82\,\text{Hz}$.

2.4.1. Radio seismic indicator relating distance and magnitude

The proposed RSI is synthesized with the following considerations and assumptions:

1. The intensity of H_ϕ is proportional to the EQ intensity as the square root of the energy; any scaling factor is absorbed by the later trimming of the threshold for detectability of precursors.
2. The estimate of H_ϕ intensity as a function of distance (i.e. the path loss) is given by the solution of the wave equations (see Fig. 1), suitably interpolated for the frequency and distance ranges of interest: the frequency is selected to cover approximately the range of observed precursors ($1\,\text{Hz}$ to $30\,\text{Hz}$); the distance is limited to planetary distances for which the estimated attenuation is acceptable, namely $15\,000\,\text{km}$ (pragmatically observing the farthest stations in the available literature data).

3. No accurate quantitative data of propagation are available for frequencies below ELF, that are commonly monitored and analyzed for precursors; in this case the propagation characteristics at the lowest ELF frequency values are used. In general, at $1\,\text{Hz}$ the wavelength is already $300\,000\,\text{km}$ in free space, much longer than planetary distances.

An exponential relationship between magnitude and energy as in (3) is assumed. In addition, the local EQ energy E'_s released during the event is assumed to be fairly constant over a time duration over which the observations are carried out. This allows replacing power with E'_s, interpreted as average energy. As synthesized in Table 2, all contributors agree on an exponent 1.5 to relate EQ energy and magnitude, and this will be followed also in the proposed RSI expression; small deviations will be verified to check the sensitivity of the classification of events to the assumed exponential relationship.

Combining the square root of energy $\sqrt{E'_s}$ and the path loss for the H_ϕ component, the expression of the proposed RSI can be derived. It is observed that the calculated exponents fitting H_ϕ path loss (between 0.874 and 1.189), once multiplied by 2 (to get back to an energy expression), bracket and roughly correspond to the exponent of 2 at the denominator of (3).

$$\text{RSI}_1 = \frac{\sqrt{M^{1.5}}}{R^{p_1}} \qquad \text{RSI}_2 = \frac{\sqrt{M^{1.5}}}{a_1 R^{p_1} + R^{p_2}} \tag{6}$$

where a_1, p_1 and p_2 result from the H_ϕ path loss fitting.

The RSI is directly comparable to the other indicators previously discussed and it is not instead comparable with the RI proposed in Romero et al. (2023) that was expressed in dBe, with "e" standing for earthquake.

3. Monitored events

This section collects all relevant seismic events considered for classification by RSI (see Table 4). The origin of data is a set of scientific publications and the Opera Project.

3.1. Literature data

Table 4 shows a synthesis of literature data available for ELF e.m. signals received by ground stations. For each EQ the following quantities were extracted: Richter magnitude M, distance R from the measuring station, frequency interval of the detected precursor. Each event has then a calculated RSI value.

Compared to Romero et al. (2023) we have reported some additional entries where the same EQ event was recorded and analyzed at different stations, so at different distances from the EQ, providing more complete information on the magnitude-distance relationships. An example is P132, where what reported in Shrivastava (2014) has been amended, indicating the more correct information of Prattes et al. (2011). Other cases are those of Opera 2015, where we have made distinction between closest and farthest stations, underlining that the analysis was done for the recorded signals of all stations.

3.2. Opera project data

The Opera 2015 project (Romero, 2015; Romero et al., 2023) carried out systematic ELF monitoring during 2015. The original RI indicator (Romero et al., 2023) had a fixed reference magnitude M_0 and warning distance R_0 selected considering that weaker seismic events are hardly detectable at long distance, but shorter distances by the way would not ensure an efficient coverage of the territory. During the project those events exceeding a magnitude threshold $M_{thr} = 3.2$ (below M_0 with some margin) were analyzed in detail for a series of spectral characteristics, similarly to the analysis in Hattori (2004a).

The measurement campaign collected data from 14 sensors, positioned in 6 different locations of high seismic activity. The monitoring stations were continuously active for a total of more than 110,000 recording hours during the project. A total of 15532 EQ detected during 2015 by the Italian Institute of Geophysics and Volcanology were evaluated, so an average of 40 EQs per day. By selecting those above M_{thr}, 279 events remained, for which the RSI was calculated. The following 41 earthquake events shown in Table 4 were selected with the highest probability of finding an associated electromagnetic emission.

3.3. Overview of collected EQ data

EQ events collected in Table 4 have been evaluated considering their distribution in the $R - M$ plane preliminarily to their use for precursors verification. The reason is verifying their compactness and suitability for clustering, probing thus possible bad behavior for the separation capability required to the indicators. Results are reported in Fig. 2 as a 2D-histogram (versus magnitude and distance) and a 1D-histogram over a convenient projection that normalizes magnitude over the logarithm of squared distance. It is noted that the positive cases are quite dispersed with overlapping intervals of 1 standard deviation, although the mean values (centers of gravity) are separated.

It is evident that full separability of groups of positive and negative precursor events is compromised by significant overlapping, both visible in the 2D histogram and in the projected 1D histogram, where the centers of gravity of the three groups (positive, negative and dubious precursor detection) are distinct, but separated much less than the sample dispersion σ within each group (indicated by the horizontal lines spanning $\pm 1\sigma$).
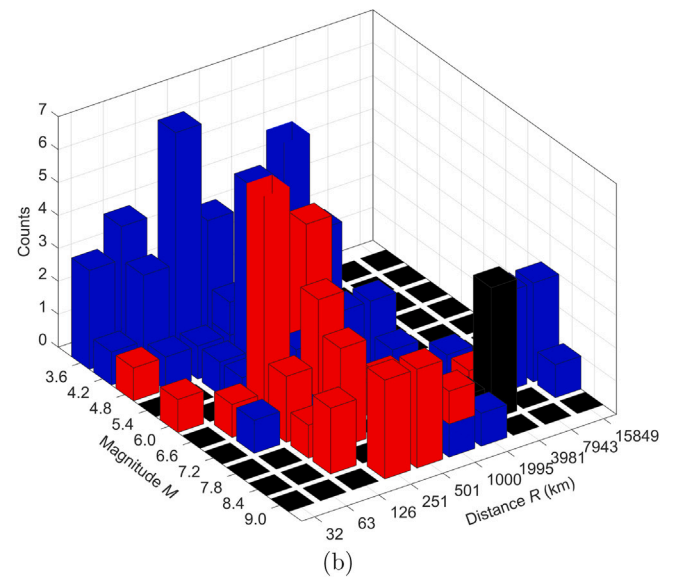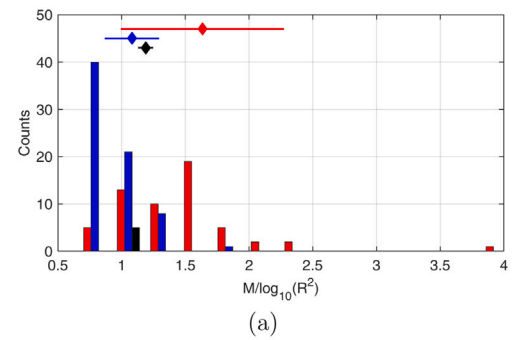

Fig. 2. Histograms of collected EQ events, subdivided as negative (blue), positive (red) and doubtful (black): (a) 1D histogram for the normalized magnitude M by assuming a standard quadratic path loss (the diamonds are the mean values of the three distributions and the horizontal lines indicate the dispersion); (b) 2D histogram using magnitude M and distance R.

4. Results and discussion

The events listed in Table 4 are reported in Fig. 3 on magnitude M and distance R axes with the following notation: reddish and bluish color for positively and negatively found precursors (with slight nuances to distinguish the frequency interval of the precursor). The indicators reviewed in Section 2.3 are also reported in various colors on the same plot. The proposed RSI is included having assigned to it a decision threshold that maximizes performance (1.0 for RSI_1 and 1.2 for RSI_2).

Visual inspection of results confirms that events and associated existence of precursors may be subdivided in three areas: one in the top-left characterized by intense EQs and short distance, where detectability of precursors is confirmed; an intermediate elongated area (inclined stripe), where positive and negative events overlap and separation is complicated; a lower bottom-right triangular area, where the intensity of the received signals is such that no precursor can be reliably detected. It is acknowledged that, especially for the intermediate part of the graph, received intensity and detectability may depend on other factors: depth of the earthquake and characteristics of the source, characteristic of the soil through which propagation to the surface occurs, amount of natural and man-made disturbance in the specific location where the monitoring station is located.

Evaluating performances of correct identification and separation is subject to different interpretations, depending on the aspect that is

Table 4
Overview of collected EQ events.

ID	Date	UTC	Location	M	R (km)	Freq.	Prec.	Symb.	Ref.
01	1964-03-28	3:36	Prince William Sound, Alaska	9.2	460	ULF	1	A	Shrivastava (2014)
02	1988-12-07	7:41	Spitak, Armenia	6.9	120	0.005–1 Hz	1	A	Shrivastava (2014)
03	1988-12-07	7:41	Spitak, Armenia	6.9	200	0.005–1 Hz	1	A	Shrivastava (2014)
04	1989-10-17	4:15	Mt. Loma Prieta, California	7.1	52	10 Hz - 32 kHz	−1	B	Fraser-Smith et al. (1990)
05	1989-10-17	4:15	Mt. Loma Prieta, California	7.1	7	0.01–10 Hz	1	B	Fraser-Smith et al. (1990)
06	1993-08-08	8:34	Guam	8.0	65	0.02–0.05 Hz	1	A	Shrivastava (2014)
07	1996-02-17	5:59	Biak, Indonesia	8.2	80	0.005–0.03 Hz	1	A	Shrivastava (2014)
08	1996-12-03	nd	Hyuganada	6.6	96	0.005 & 0.03 Hz	1	C	Akinaga et al. (2000)
09	1997-03-26	8:31	Kyushu, Kagoshima, Japan	6.5	64	0.005 & 0.03 Hz	1	C	Akinaga et al. (2000)
10	1997-05-13	5:38	Kyushu, Kagoshima, Japan	6.3	64	0.005 & 0.03 Hz	1	C	Akinaga et al. (2000)
11	1998-05-03	nd	Izu Swarm	5.7	30	10-30 mHz	1	D	Hattori (2004a)
12	1998-07-01	nd	near Matshshiro	4.5	25	10-30 mHz	1	D	Hattori (2004a)
13	1998-09-03	nd	Iwateken Nairiku-Hokubu, Japan	6.1	15	5-10 mHz	1	D	Hattori (2004a)
14	1998-09-03	7:58	Iwateken Nairiku-Hokubu, Japan	6.1	15	10-50 mHz	1	E	Hattori (2004b)
15	1999-09-21	17:47	Chi-chi, Taiwan	7.6	2000	26 Hz	1	F	Hayakawa et al. (2005)
16	1999-09-21	17:47	Chi-chi, Taiwan	7.7	135	10 mHz	1	D	Hattori (2004a)
17	2000-07-01	7:01	Izu Island, Japan	6.5	83	0.1 Hz	1	G	Hattori et al. (2006)
18	2000-07-08	18:57	Izu Island, Japan	6.1	82	0.1 Hz	1	G	Hattori et al. (2006)
19	2000-07-15	1:30	Izu Island, Japan	6.3	62	0.1 Hz	1	G	Hattori et al. (2006)
20	2000-07-30	0:28	Izu Island, Japan	6.0	107	0.1 Hz	1	G	Hattori et al. (2006)
21	2000-07-30	12:25	Izu Island, Japan	6.5	113	0.1 Hz	1	G	Hattori et al. (2006)
22	2000-08-18	1:52	Izu Island, Japan	6.1	84	0.1 Hz	1	G	Hattori et al. (2006)
23	2004-10-23	8:56	Mid-Niigata, Japan	6.8	250	16.3 Hz	1	H	Hayakawa et al. (2005)
24	2005-10-08	nd	Muzaffarabad, Kashmir, Pakistan	7.7	908	2 & 7–8 Hz	1	I	Kushwah et al. (2007)
25	2006-11-15	nd	Kurile Island, Japan	8.3	2520	0.03–0.05 Hz	0	J	Schekotov and Hayakawa (2014)
26	2006-11-15	nd	Kurile Island, Japan	8.3	750	0.03–0.05 Hz	1	J	Schekotov and Hayakawa (2014)
27	2006-11-15	nd	Kurile Island, Japan	8.3	1540	0.03–0.05 Hz	−1	J	Schekotov and Hayakawa (2014)
28	2007-02-24	19:47	Kamchatka peninsula, Russia	5.4	839	0.1–30 Hz	−1	K	Hayakawa et al. (2012)
29	2007-03-02	20:14	Kamchatka peninsula, Russia	4.9	338	0.1–30 Hz	1	K	Hayakawa et al. (2012)
30	2007-03-06	nd	Singkarak, Sumatra	6.4	79	0.06 Hz	1	L	Ahadi et al. (2015)
31	2007-03-07	20:14	Kamchatka peninsula, Russia	4.8	404	0.1–30 Hz	−1	K	Hayakawa et al. (2012)
32	2007-03-11	7:09	Kamchatka peninsula, Russia	5.8	450	0.1–30 Hz	1	K	Hayakawa et al. (2012)
33	2007-03-17	11:40	Kamchatka peninsula, Russia	4.8	374	0.1–30 Hz	−1	K	Hayakawa et al. (2012)
34	2007-03-18	1:25	Kamchatka peninsula, Russia	5.5	283	0.1–30 Hz	1	K	Hayakawa et al. (2012)
35	2007-03-25	0:41	Kamchatka peninsula, Russia	6.7	915	0.1–30 Hz	1	K	Hayakawa et al. (2012)
36	2007-03-25	0:41	Noto-Hantou peninsula, Japan	6.9	200	20.7 Hz	1	H	Hayakawa et al. (2010)
37	2007-03-29	21:07	Kamchatka peninsula, Russia	5.4	912	0.1–30 Hz	−1	K	Hayakawa et al. (2012)
38	2007-07-22	nd	India/Pakistan/Nepal area	5.1	408	0.01–30 Hz	−1	M	Chauhan et al. (2009)
39	2007-08-01	nd	India/Pakistan/Nepal area	4.5	467	0.01–30 Hz	1	M	Chauhan et al. (2009)
40	2007-09-12	nd	Bengkulu, Sumatra	8.5	526	0.06 Hz	1	L	Ahadi et al. (2015)
41	2007-10-04	nd	India/Pakistan/Nepal area	4.6	628	0.01–30 Hz	1	M	Chauhan et al. (2009)
42	2007-11-10	nd	Pagai Selatan, Sumatra	5.9	386	0.06 Hz	1	L	Ahadi et al. (2015)
43	2007-11-25	nd	India/Pakistan/Nepal area	4.7	172	0.01–30 Hz	1	M	Chauhan et al. (2009)
44	2007-12-02	nd	Pagai Utara, Sumatra	5.3	275	0.06 Hz	1	L	Ahadi et al. (2015)
45	2008-05-12	6:28	Wenchuang, China	7.9	1251	0.01–30 Hz	0	N	Chauhan et al. (2012)
46	2008-05-12	6:28	Wenchuang, China	7.9	2376	0.01–30 Hz	0	N	Chauhan et al. (2012)
47	2008-05-12	6:28	Wenchuang, China	7.9	2496	0.01–30 Hz	0	N	Chauhan et al. (2012)
48	2008-05-12	6:28	Wenchuang, China	7.9	3368	0.01–30 Hz	0	N	Chauhan et al. (2012)
49	2008-05-19	nd	Sipirok, Sumatra	6.0	205	0.06 Hz	1	L	Ahadi et al. (2015)
50	2009-01-28	nd	Hibala, Sumatra	5.7	233	0.06 Hz	1	L	Ahadi et al. (2015)
51	2009-04-06	01:32	L'Aquila, Italy	6.3	5	10–15 mHz	1	W	Prattes et al. (2011)
52	2009-04-06	01:32	L'Aquila, Italy	6.3	420	10–15 mHz	−1	W	Prattes et al. (2011)
53	2009-06-14	nd	South of Bandung, Java	5.0	156	ULF	−1	P	Febriani et al. (2014)
54	2009-08-16	nd	Mentawai, Sumatra	6.7	208	0.06 Hz	1	L	Ahadi et al. (2015)
55	2009-09-02	nd	South of Bandung, Java	6.0	142	ULF	−1	P	Febriani et al. (2014)
56	2009-09-02	nd	South of Bandung, Java	5.1	150	ULF	−1	P	Febriani et al. (2014)
57	2009-09-02	nd	South of Bandung, Java	5.3	144	ULF	−1	P	Febriani et al. (2014)
58	2009-09-09	nd	Java Island	7.5	135	0.01 ± 0.003 Hz	1	P	Febriani et al. (2014)
59	2009-09-13	nd	South of Bandung, Java	6.6	126	ULF	−1	P	Febriani et al. (2014)
60	2009-09-28	nd	South of Bandung, Java	5.3	144	ULF	−1	P	Febriani et al. (2014)
61	2009-09-30	nd	Padang, Sumatra	7.6	114	0.06 Hz	1	L	Ahadi et al. (2015)
62	2009-10-08	nd	South of Bandung, Java	5.1	144	ULF	−1	P	Febriani et al. (2014)
63	2009-10-24	nd	South of Bandung, Java	5.1	145	ULF	−1	P	Febriani et al. (2014)
64	2010-02-20	nd	South of Bandung, Java	5.0	95	ULF	−1	P	Febriani et al. (2014)
65	2010-05-15	nd	South of Bandung, Java	6.0	154	ULF	−1	P	Febriani et al. (2014)
66	2010-07-24	nd	Siabu, Sumatra	5.3	124	0.06 Hz	1	L	Ahadi et al. (2015)
67	2010-08-11	nd	South of Bandung, Java	5.5	105	ULF	−1	P	Febriani et al. (2014)
68	2010-10-25	nd	Mentawai, Sumatra	7.8	424	0.06 Hz	1	L	Ahadi et al. (2015)
69	2011-03-11	5:46	Tohoku, Japan	8.9	170	0.01–0.033 Hz	1	R	Kopytenko et al. (2012)
70	2011-03-11	5:46	Tohoku, Japan	8.9	200	0.01–0.033 Hz	1	R	Kopytenko et al. (2012)
71	2011-03-11	5:46	Tohoku, Japan	8.9	300	0.01–0.033 Hz	1	R	Kopytenko et al. (2012)
72	2011-03-11	5:46	Tohoku, Japan	8.9	420	0.01–0.033 Hz	1	R	Kopytenko et al. (2012)
73	2011-03-11	5:46	Tohoku, Japan	9.0	642	0.001–0.1 Hz	1	S	Kanata et al. (2014)

(*continued on next page*)

Table 4 (*continued*).

ID	Date	UTC	Location	M	R (km)	Freq.	Prec.	Symb.	Ref.
74	2011-03-11	5:46	Tohoku, Japan	9.0	301	0.001–0.1 Hz	1	S	Kanata et al. (2014)
75	2011-03-11	5:46	Tohoku, Japan	9.0	1295	0.001–0.1 Hz	1	S	Kanata et al. (2014)
76	2011-03-11	5:46	Tohoku, Japan	9.0	850	<1 Hz	−1	T	Contoyiannis et al. (2016)
77	2011-03-11	5:46	Tohoku, Japan	9.0	1200	<1 Hz	−1	T	Contoyiannis et al. (2016)
78	2011-03-11	5:46	Tohoku, Japan	9.0	250	<1 Hz	1	T	Contoyiannis et al. (2016)
79	2012-06-23	nd	Kutacane, Sumatra	6.1	411	0.06 Hz	1	L	Ahadi et al. (2015)
80	2016-03-20	nd	Kuril–Kamchatka, Russia	6.7	362	ULF	1	U	Schekotov et al. (2020)
81	2016-03-22	nd	Kuril–Kamchatka, Russia	5.0	364	ULF	−1	U	Schekotov et al. (2020)
82	2016-03-25	nd	Kuril–Kamchatka, Russia	5.5	366	ULF	−1	U	Schekotov et al. (2020)
83	2016-04-05	nd	Kuril–Kamchatka, Russia	5.5	320	ULF	1	U	Schekotov et al. (2020)
84	2016-04-14	nd	Kuril–Kamchatka, Russia	6.2	219	ULF	1	U	Schekotov et al. (2020)
85	2016-04-15	16:25	Kumamoto, Kyusyu is., Japan	7.3	150	10 - 20 mHz	1	V	Schekotov et al. (2017)
86	2016-04-16	nd	Kuril–Kamchatka, Russia	5.1	468	ULF	−1	U	Schekotov et al. (2020)
87	2016-04-22	nd	Kuril–Kamchatka, Russia	5.1	539	ULF	−1	U	Schekotov et al. (2020)
88	2016-05-05	nd	Kuril–Kamchatka, Russia	5.4	375	ULF	1	U	Schekotov et al. (2020)
89	2015-01-10	23:50:02	South Sicily channel, Italy	3.9	243	0.1–30 Hz	−1	Z	Romero (2015)
90	2015-01-23	06:51:20	Bologna, Italy	4.3	60	0.1–30 Hz	−1	Z	Romero (2015)
91	2015-01-28	15:54:37	Crete, Greece	5.2	974	0.1–30 Hz	−1	Z	Romero (2015)
92	2015-02-06	08:52:27	Eolie Islands, Italy	4.7	119	0.1–30 Hz	−1	Z	Romero (2015)
93	2015-02-13	18:59:16	Northern Mid-Atlantic Ridge	6.8	2935	0.1–30 Hz	−1	Z	Romero (2015)
94	2015-02-17	19:42:53	Florence, Italy	3.7	42	0.1–30 Hz	−1	Z	Romero (2015)
95	2015-03-04	00:00:04	Florence, Italy	3.7	92	0.1–30 Hz	−1	Z	Romero (2015)
96	2015-03-27	23:34:54	Crete, Greece [Sea]	5.4	1056	0.1–30 Hz	−1	Z	Romero (2015)
97	2015-03-29	10:48:46	Calabria S-E coast, Italy"	3.6	116	0.1–30 Hz	−1	Z	Romero (2015)
98	2015-03-29	23:48:30	New Britain, Papua, New Guinea	7.6	14184	0.1–30 Hz	−1	Z	Romero (2015)
99	2015-04-01	04:58:11	Ravenna, Italy	3.2	38	0.1–30 Hz	−1	Z	Romero (2015)
100	2015-04-11	05:33:13	Italy-France border	3.2	78	0.1–30 Hz	−1	Z	Romero (2015)
101	2015-04-16	18:07:43	Crete, Greece [Sea]	6.4	1090	0.1–30 Hz	−1	Z	Romero (2015)
102	2015-04-20	01:07:43	Catania, Italy	3.6	23	0.1–30 Hz	−1	Z	Romero (2015)
103	2015-04-24	15:02:53	Ravenna, Italy	4.0	37	0.1–30 Hz	−1	Z	Romero (2015)
104	2015-04-25	06:11:26	Nepal	7.7	6446	0.1–30 Hz	−1	Z	Romero (2015)
105	2015-05-12	07:05:20	Nepal	7.3	6592	0.1–30 Hz	−1	Z	Romero (2015)
106	2015-05-24	06:00:32	Reggio Calabria, Italy	3.9	96	0.1–30 Hz	−1	Z	Romero (2015)
107	2015-05-29	13:07:56	Teramo coast, Italy	4.2	207	0.1–30 Hz	−1	Z	Romero (2015)
108	2015-05-30	11:23:02	Bonin Islands, Japan [Sea]	7.6	10455	0.1–30 Hz	−1	Z	Romero (2015)
109	2015-06-09	01:09:03	Greece [Sea]	5.1	736	0.1–30 Hz	−1	Z	Romero (2015)
110	2015-06-09	21:49:49	Crete, Greece [Sea]	5.4	1087	0.1–30 Hz	−1	Z	Romero (2015)
111	2015-07-22	12:57:43	Bologna, Italy	3.7	72	0.1–30 Hz	−1	Z	Romero (2015)
112	2015-08-02	06:58:05	Calabria N-W coast, Italy	4.0	206	0.1–30 Hz	−1	Z	Romero (2015)
113	2015-08-03	07:27:49	Cosenza, Italy	4.0	212	0.1–30 Hz	−1	Z	Romero (2015)
114	2015-08-24	03:43:53	Ravenna, Italy	3.5	38	0.1–30 Hz	−1	Z	Romero (2015)
115	2015-08-29	18:47:03	Italy-Slovenia border	4.0	251	0.1–30 Hz	−1	Z	Romero (2015)
116	2015-09-10	07:32:08	Turin, Italy	3.1	27	0.1–30 Hz	−1	Z	Romero (2015)
117	2015-09-13	01:04:34	Florence, Italy	3.8	88	0.1–30 Hz	−1	Z	Romero (2015)
118	2015-09-16	22:54:33	Central coast, Chile	8.2	11641	0.1–30 Hz	−1	Z	Romero (2015)
119	2015-09-19	07:12:47	Pesaro and Urbino, Italy	3.7	38	0.1–30 Hz	−1	Z	Romero (2015)
120	2015-09-18	19:24:52	Pesaro and Urbino, Italy	3.5	37	0.1–30 Hz	−1	Z	Romero (2015)
121	2015-09-20	22:27:58	Siracusa coast, Italy	3.8	74	0.1–30 Hz	−1	Z	Romero (2015)
122	2015-10-20	10:35:50	Modena, Italy	3.5	59	0.1–30 Hz	−1	Z	Romero (2015)
123	2015-10-26	09:09:32	Hindu Kush, Afghanistan	7.5	4878	0.1–30 Hz	−1	Z	Romero (2015)
124	2015-11-01	07:52:34	Slovenia-Croatia border	4.8	340	0.1–30 Hz	−1	Z	Romero (2015)
125	2015-11-06	04:03:04	Italy-France border	3.8	78	0.1–30 Hz	−1	Z	Romero (2015)
126	2015-11-20	05:12:24	Greek-Ionic coast	5.0	485	0.1–30 Hz	−1	Z	Romero (2015)
127	2015-11-18	12:15:39	Greek-Ionic coast	5.0	509	0.1–30 Hz	−1	Z	Romero (2015)
128	2015-11-17	08:33:46	Greek-Ionic coast	5.3	494	0.1–30 Hz	−1	Z	Romero (2015)
129	2015-11-17	07:10:08	Greek-Ionic coast	6.5	496	0.1–30 Hz	−1	Z	Romero (2015)
130	2015-11-24	22:50:54	Peru-Brazil border	7.6	9893	0.1–30 Hz	−1	Z	Romero (2015)
131	2015-12-08	10:53:55	Catania, Italy	3.2	20	0.1–30 Hz	−1	Z	Romero (2015)
132	2015-12-08	09:28:30	Catania, Italy	3.4	19	0.1–30 Hz	−1	Z	Romero (2015)
133	2015-12-20	09:46:03	North Sicilian coast, Italy	4.2	150	0.1–30 Hz	−1	Z	Romero (2015)

deemed more relevant: identifying conditions for existence of precursors (maximizing identification of positive EQ events); avoiding waste of time processing events for which there are no suitable conditions (minimizing identification of negative EQ events); balancing the two, separating at best positive and negative events with minimal confusion. From this the classification performance can be evaluated by calculating the confusion matrix.

The confusion matrix summarizes the results of a classification problem by counting the number of correct and incorrect predictions for each class, having selected positive and negative precursor existence as classes in the present problem. Results are classified as True Positive (TP), True Negative (TN), False Positive (FP) and False Negative (FN),

as shown in Fig. 4. Of the entire set of positive precursors indicated by P, the ratio of those truly classified as positive TP defines the hit ratio (or "sensitivity"): TP/P. Symmetrically, the performance for negative cases is named "specificity" and expressed as TN/N. The concept of minimizing FP may reflect into "precision" $TP/(TP + FP)$ (if weighted against TPs) or "fall-out rate" $FP/N = FP/(FP + TN)$ (considering FPs as negative cases leaked, or fallen out, into a positive classification). A common objective is the minimization of off-diagonal terms, that is improving separation by reducing falling-out cases to the minimum.
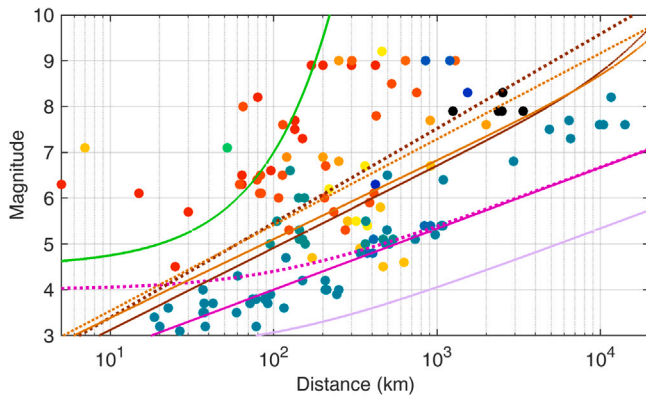
Fig. 3. Magnitude-Distance plot of EQ events and precursors indicators: reddish and bluish dots for positive and negative precursors of Table 4, black dots for the few doubtful events. Past indicators are Hattori ((1), green), Molchanov1 and Molchanov3 ((2), magenta solid and dashed), Molchanov2 ((2), violet). Proposed RSI: RSI$_1$ (brownish dashed) and RSI$_2$ (brownish solid), referred to c_1 (darker) and c_{12} (lighter) approximations; threshold values are 1.0 and 1.2 for maximized classification performance, then shown in Fig. 5.

Fig. 4. Graphical description of the confusion matrix.

A first measure of performance is the balanced accuracy (BA), combining the correct classification for both positive and negative cases (thus weighting TP and TN values):

$$BA = \frac{1}{2}\left(\frac{TP}{P} + \frac{TN}{N}\right) = \frac{1}{2}\left(\frac{n_{11}}{n_{1\Sigma}} + \frac{n_{00}}{n_{0\Sigma}}\right) \tag{7}$$

Other performance indexes, used e.g. for medical diagnostics, tend to privilege conservatively efficacy on positive cases, such as the diagnostic odds ratio. Here attention is focused on indexes giving an overall and balanced metric of performance.

Being possible the classes of positive and negative precursor outcomes of much different size, the ϕ coefficient shown in (8) turns out to be another effective measure of the goodness of performance. Such index, also known as Matthews' coefficient, contains the difference of

the product of diagonal and off-diagonal terms, indicating situations where sensitivity (or specificity) is maximized and fall-out rate is minimized.

$$\phi = \frac{TP \times TN - FP \times FN}{\sqrt{(TP+FN)(FP+TN)(TP+FP)(FN+TN)}}$$
$$= \frac{n_{11}n_{00} - n_{01}n_{10}}{\sqrt{n_{1\Sigma}n_{0\Sigma}n_{\Sigma1}n_{\Sigma0}}} \tag{8}$$

Performance results in terms of both ϕ and BA are shown in Fig. 5 for past indicators and the proposed RSI. The range of both metrics is between 0 and 1. The RSI performs best for both BA and ϕ. The second-order RSI model improves, although marginally, the separation of events with a slightly better slope, particularly useful in the center of the graph of Fig. 3. An intrinsic limitation to reach unity and maximize performance lies in the lack of separability of the original data, with overlapping of positive and negative findings.

5. Conclusion

This work has selected a set of the most representative EQs of the last 25 years documenting their main characteristics. To these first 87, another strong 40 events recorded during the Opera 2015 project have been added: the events were of lesser intensity and after the analysis of the recorded signals no precursor could be identified, so that they are retained as "negative" events. These Opera 2015 events beef up the set of literature negative results that tend to be very few, as publications tend to propose new findings and demonstrate them with positive hits.

A Radio-Seismic Index (RSI) has been built using the minimum information of distance and intensity of the EQ (and thus its energy and the supposed intensity of the source of e.m. waves). A propagation model was considered estimating path loss for the range of frequency and distance of interest. The model was obtained by curve fitting of published accurate expressions (Li and Pan, 2014).

The proposed RSI, together with other indicators available in past publications, has been then used to classify the events as for the detectability of precursors. The separability of the original events is initially commented; results are shown on a magnitude-distance graph. Classification and separation performances are then evaluated by means of confusion matrices (showing the ratio of the four categories of true positive and negative and false positive and negative). Parameter ϕ, also known as Matthews' coefficient, synthesizes classification performance showing an improvement of the RSI by 40% to 100% with respect to published indicators.

Visual inspection of results confirms that events and associated existence of precursors may be subdivided in three areas (see Fig. 3): one in the top-left characterized by intense EQs and short distance, where detectability of precursors is confirmed; an intermediate elongated area (an inclined stripe), where positive and negative events overlap and separation is not possible; a lower bottom-right triangular

Fig. 5. Classification performance as confusion matrices for past indicators and proposed RSI. For the latter the selected threshold values shown between parentheses are optimal for classification performance.

area where the intensity of the received signals is such that no precursor can be reliably detected. It is acknowledged that, especially for the intermediate part of the graph, received intensity and detectability may depend on other factors, for example depth of the earthquake and characteristics of the source, characteristic of the soil through which propagation to the surface occurs, and amount of natural and man-made disturbance at the specific location where the monitoring station is located.

CRediT authorship contribution statement

Andrea Mariscotti: Conceptualization, Formal analysis, Methodology, Writing – original draft, Writing – review & editing, Software. **Renato Romero:** Conceptualization, Data curation, Writing – original draft, Writing – review & editing, Methodology.

Declaration of Generative AI and AI-assisted technologies in the writing process

No AI and AI-assisted technologies were used.

Declaration of competing interest

The authors declare that they have no known competing financial interests or personal relationships that could have appeared to influence the work reported in this paper.

References

Ahadi, S., Puspito, N., Ibrahim, G., Saroso, S., Yumoto, K., Muzli, M., 2015. Anomalous ULF emissions and their possible association with the strong earthquakes in Sumatra, Indonesia, during 2007–2012. J. Math. Fundam. Sci. 47 (1), 84–103. http://dx.doi.org/10.5614/j.math.fund.sci.2015.47.1.7.

Akinaga, Y., Hattori, K., Hayakawa, M., Yumoto, K., 2000. ULF emissions associated with earthquakes in Kyushu. Int. Symp. Antennas Propag. 99 (389), 36–46. http://dx.doi.org/10.34385/proc.9.1F2-5.

Bahar, E., Wait, J.R., 1965. Propagation in a model terrestrial waveguide of nonuniform height: Theory and experiment. Radio Sci. 69 (11), 1445–1463.

Bannister, P., 1984. ELF propagation update. IEEE J. Ocean. Eng. 9 (3), 179–188. http://dx.doi.org/10.1109/JOE.1984.1145609.

Bannister, P., Wolkoff, E., Katan, J., Williams, F., 1973. Far-field, extremely-low-frequency propagation measurement. Radio Sci. 8 (7), 623–632. http://dx.doi.org/10.1029/RS008i007p00623.

Bath, M., 1966. In: Ahrens, L.H., Press, F., Runcorn, S. (Eds.), Physics and Chemistry of the Earth. Pergamon Press, pp. 115–165.

Bormann, P., Giacomo, D., 2010. The moment magnitude and the energy magnitude: common roots and differences. J. Seismol. 15 (2), 411–427. http://dx.doi.org/10.1007/s10950-010-9219-2.

Chauhan, V., Singh, O., Kushwaha, V., Singha, V., Singh, B., 2009. Ultra-low-frequency (ULF) and total electron content (TEC) anomalies observed at Agra and their association with regional earthquakes. J. Geodyn. 48 (2), 68–74. http://dx.doi.org/10.1016/j.jog.2009.06.002.

Chauhan, V., Singh, O., Pandey, U., Singh, B., Arrora, B., Rawat, G., Pathan, B., Sinha, A., Sharma, A., Patil, A., 2012. A search for precursors of earthquakes from multi-station ULF observations and TEC measurements in India. Indian J. Radio Space Phys. 41, 543–556.

Contoyiannis, Y., Potirakis, S., Eftaxias, K., Hayakawa, M., Schekotov, A., 2016. Intermittent criticality revealed in ULF magnetic fields prior to the 11 March 2011 Tohoku earthquake (Mw=9). Physica A http://dx.doi.org/10.1016/j.physa.2016.01.065.

Febriani, F., Han, P., Yoshino, C., Hattori, K., Nurdiyanto, B., Effendi, N., Maulana, I., Gaffar, E., 2014. Ultra low frequency (ULF) electromagnetic anomalies associated with large earthquakes in Java Island, Indonesia by using wavelet transform and detrended fluctuation analysis. Nat. Hazards Earth Syst. Sci. 14 (4), 789–798. http://dx.doi.org/10.5194/nhess-14-789-2014.

Fraser-Smith, A., Bannister, P., 1998. Reception of ELF signals at antipodal distances. Radio Sci. 33 (1), 83–88. http://dx.doi.org/10.1029/97RS01948.

Fraser-Smith, A., Bernardi, A., McGill, P., Ladd, M., Helliwell, R., Villard, Jr., O., 1990. Low-frequency magnetic field measurements near the epicenter of the Ms 7.1 Loma Prieta earthquake. Geophys. Res. Lett. 17 (9), 1465–1468. http://dx.doi.org/10.1029/GL017i009p01465.

Han, P., Hattori, K., Zhuang, J., Chen, C.H., Liu, J.Y., Yoshida, S., 2017. Evaluation of ULF seismo-magnetic phenomena in Kakioka, Japan by using Molchan's error diagram. Geophys. J. Int. 208, 482–490. http://dx.doi.org/10.1093/gji/ggw404.

Hattori, K., 2004a. ULF geomagnetic changes associated with large earthquakes. Terr. Atmospheric Ocean. Sci. 15 (3), 329–360. http://dx.doi.org/10.3319/TAO.2004.15.3.329(EP).

Hattori, K., 2004b. ULF geomagnetic field measurements in Japan and some recent results associated with Iwateken Nairiku Hokubu earthquake in 1998. Phys. Chem. Earth 29, 481–494. http://dx.doi.org/10.1016/j.pce.2003.09.019.

Hattori, K., Serita, A., Yoshino, C., Hayakawa, M., Isezaki, N., 2006. Singular spectral analysis and principal component analysis for signal discrimination of ULF geomagnetic data associated with 2000 Izu Island Earthquake Swarm. Phys. Chem. Earth 31 (4–9), 281–291. http://dx.doi.org/10.1016/j.pce.2006.02.034.

Hayakawa, M., Ohta, K., Nickolaenko, A., Ando, Y., 2005. Anomalous effect in Schumann resonance phenomena observed in Japan, possibly associated with the Chi-Chi earthquake in Taiwan. Ann. Geophys. 23 (4), 1335–1346. http://dx.doi.org/10.5194/angeo-23-1335-2005.

Hayakawa, M., Ohta, K., Sorokin, V., Yaschenko, A., Izutsu, J., Hobara, Y., Nickolaenko, A., 2010. Interpretation in terms of gyrotropic waves of Schumann-resonance-like line emissions observed at Nakatsugawa in possible association with nearby Japanese earthquakes. J. Atmos. Sol.-Terr. Phys. 72 (17), 1292–1298. http://dx.doi.org/10.1016/j.jastp.2010.09.014.

Hayakawa, M., Schekotov, A., Molchanov, O., Hobara, Y., 2012. Estimation of the efficiency of combined characteristics of ULF-ELF fields as a precursor to earthquakes based on the observations in February-March 2007 in Moshiri. J. Atmospheric Electr. 32 (1), 35–40.

Heavlin, W.D., Kappler, K., Yang, L., Fan, M., Hickey, J., Lemon, J., MacLean, L., Bleier, T., Riley, P., Schneider, D., 2022. Case-control study on a decade of ground-based magnetometers in california reveals modest signal 24–72 hr prior to earthquakes. J. Geophys. Res. Solid Earth 127 (10), http://dx.doi.org/10.1029/2022jb024109.

ITU-T Std. B.15, 1996. Nomenclature of the frequency and wavelength bands used in telecommunications.

Johnston, M.J.S., Mueller, R.J., Keller, V., 1981. Preseismica nd coseismicm agnetic field MeasurementsN ear the coyote lake, California, Earthquake of August 6, 1979. J. Geophys. Res. 86 (B2), 921–926.

Kanata, B., Zubaidah, T., Ramadhani, C., Irmawati, B., 2014. Changes of the geomagnetic signals linked to Tohoku earthquake on March 11th 2011. Int. J. Technol. 5 (3), 251–258. http://dx.doi.org/10.14716/ijtech.v5i3.611.

Kopytenko, Y., Ismaguilov, V., Hattori, K., Hayakawa, M., 2012. Anomaly disturbances of the magnetic fields before the strong earthquake in Japan on March 11, 2011. Ann. Geophys. 55 (1), http://dx.doi.org/10.4401/ag-5260.

Kushwah, V., Singh, V., Singh, B., 2007. Ultra Low Frequency (ULF) amplitude anomalies associated with the recent Pakistan earthquake of 8 October, 2005. J. Indian Geophys. Union 11 (4), 197–207.

Li, K., Pan, W., 2014. Propagation of SLF/ELF Electromagnetic Waves. Springer.

Molchanov, O., Schekotov, A., Solovieva, M., Fedorov, E., Gladyshev, V., Gordeev, E., Chebrov, V., Saltykov, D., Sinitsin, V., Hattori, K., Hayakawa, M., 2005. Near-seismic effects in ULF fields and seismo-acoustic emission: statistics and explanation. Nat. Hazards Earth Syst. Sci. 5, 1–10. http://dx.doi.org/10.5194/nhess-5-1-2005.

Ohta, K., Izutsu, J., Schekotov, A., Hayakawa, M., 2013. The ULF/ELF electromagnetic radiation before the 11 March 2011 Japanese earthquake. Radio Sci. 48, 589–596. http://dx.doi.org/10.1002/rds.20064.

Peng, H., Tao, W., Pan, W., Guo, L., 2012. Numerical integral method for ELF fields excited by vertical electric dipole in asymmetric earth-ionosphere cavity. Chin. J. Radio Sci..

Prattes, G., Schwingenschuh, K., Eichelberger, H.U., Magnes, W., Boudjada, M., Stachel, M., Vellante, M., Villante, U., Wesztergom, V., Nenovski, P., 2011. Ultra low frequency (ULF) European multi station magnetic field analysis before and during the 2009 earthquake at L'Aquila regarding regional geotechnical information. Nat. Hazards Earth Syst. Sci. 11 (7), 1959–1968. http://dx.doi.org/10.5194/nhess-11-1959-2011.

Romero, R., 2015. Osservatorio permanente emissioni radiosismiche (radio-seismic emission permanent observatory). URL: http://www.vlf.it/opera_2015/opera_2015.html.

Romero, R., Feletti, L., Re, C., Mariscotti, A., 2023. Opera 2015 project: Accurate measurement equipment for earthquake electromagnetic emissions and radio seismic indicator. Sensors 23 (5), 2379. http://dx.doi.org/10.3390/s23052379.

Schekotov, A., Chebrov, D., Hayakawa, M., Belyaev, G., Berseneva, N., 2020. Short-term earthquake prediction in Kamchatka using low-frequency magnetic fields. Nat. Hazards 100, 735–755. http://dx.doi.org/10.1007/s11069-019-03839-2.

Schekotov, A., Fedorov, E., Molchanov, O., Hayakawa, M., 2013. Low frequency electromagnetic precursors as a prospect for earthquake prediction. In: Hayakawa, M. (Ed.), Earthquake Prediction Studies: Seismo Electromagnetics. Terrapub, pp. 81–99.

Schekotov, A., Hayakawa, M., 2014. Ultra-low-frequency magnetic field depression for three huge oceanic earthquakes in Japan and in the Kurile islands. In: Proc. of the IEICE Intern. Symp. on Electromagnetic Compatibility. Tokyo, Japan, http://dx.doi.org/10.34385/proc.18.13a-s3.

Schekotov, A., Izutsu, J., Asano, T., Potirakis, S., Hayakawa, M., 2017. Electromagnetic precursors to the 2016 Kumamoto earthquakes. Open J. Earthq. Res. 6, 168–179. http://dx.doi.org/10.4236/ojer.2017.64010.

Shrivastava, A., 2014. Are pre-seismic ULF electromagnetic emissions considered as a reliable diagnostics for earthquake prediction? Current Sci. 107 (4), 596–600, URL: https://www.jstor.org/stable/24103531.

Straser, V., 2011. Radio wave anomalies, ULF geomagnetic changes and variations in the interplanetary magnetic field preceding the Japanese M9.0 earthquake. New Concepts Glob. Tectonics Newsl. (59), 78.

Straser, V., 2012. Intervals of pulsation of diminishing periods and radio anomalies found before the occurrence of M6+ earthquakes. New Concepts Glob. Tectonics Newsl. (65), 35, URL: lhttp://users.neo.registeredsite.com/6/9/1/18560196/assets/ncgt65_Dec2012_.pdf.

Straser, V., Cataldi, G., 2014. Solar Wind Proton Density Increase and Geomagnetic Background Anomalies Before Strong M6+ Earthquakes. Technical Report, Space research institute of Moscow, Russian Academy of Sciences.

University of California, Los Angeles, 2017. Kelly kiloton index of earthquake moment magnitudes. https://english.ucla.edu/wp-content/uploads/Earthquake-KKI-17-1.pdf, URL: https://english.ucla.edu/wp-content/uploads/Kiloton.pdf.

Wait, J., 1960. Terrestrial propagation of very-low-frequency radio waves. J. Res. Natl. Bureau Stand. D Radio Propag. 64D (2), 153–204.

Watt, A., 1967. VLF Radio Engineering. Pergamon Press.